Axisymmetric internal wave tunneling

S. Boury ,[1,2,3] B. R. Sutherland ,[4] S. Joubaud ,[5] T. Peacock ,[6] and P. Odier [5]
[1]Université Paris Cité, Université Paris Cité, CNRS, MSC, 75013 Paris, France
[2]Université Paris-Saclay, CNRS, FAST, 91405 Orsay, France
[3]Courant Institute of Mathematical Sciences, New York University, New York, New York 10012, USA
[4]Departments of Physics and of Earth and Atmospheric Sciences, University of Alberta, Edmonton, Alberta, T6G 2E1, Canada
[5]ENS de Lyon, CNRS, Laboratoire de Physique, F-69342 Lyon, France
[6]Department of Mechanical Engineering, Massachusetts Institute of Technology, Cambridge, Massachusetts 02139, USA

(Received 31 May 2024; accepted 12 November 2024; published 9 December 2024)

Though internal waves cannot propagate vertically through weakly stratified fluid, if the depth of the weak stratification is sufficiently shallow, these waves can partially reflect from and transmit through it. In this paper, we quantitatively extend the results of Sutherland and Yewchuk [J. Fluid Mech. **511**, 125 (2004)] on Cartesian internal wave tunneling to the case of axisymmetric wave fields and discuss their tunneling through a weakly stratified layer. A simple three-layer model allowing for the computation of transmission coefficients for the velocity fields is proposed and tested on a case study. We notably show that there exists a smooth transition between the fully propagating and the tunneling regimes. We further reflect on the challenges set by the measurement of internal wave mode amplitudes in confined domains, and we discuss an innovative method to measure said amplitudes in this experimental and numerical context.

DOI: 10.1103/PhysRevFluids.9.124801

I. INTRODUCTION

Internal gravity waves propagate in density-stratified fluids such as the atmosphere and the oceans. The linear regime of these waves has been extensively studied in nonrotating linearly stratified Boussinesq fluids, i.e., in fluids of constant vertical density gradient $\partial_z \rho$ and thus of constant buoyancy frequency N. Recently, pioneering works have shown the crucial interplay between internal wave propagation and nonlinear stratifications for energy transfer purposes [1–4]. This is particularly relevant for oceanic stratifications comprising weakly stratified regions (as mentioned in [5–7]), from isolated layers to intricate staircase stratifications [8]. Examples of such stratifications have been observed both in warm regions (e.g,. in the Tyrrhenian Sea [9,10] and in the Caribbean Sea [11–13]) and cold regions (for instance, in the Arctic Ocean [8,14–17]). The latter example is of primary relevance as the shrinking ice coverage of the Arctic leads to enhanced generation of internal waves by wind-driven events at the ocean surface, which can propagate through the stratification [14,18,19], and transport energy toward the abyss.

While most of these studies have been focusing on Cartesian plane waves, they have been quantitatively extended in laboratory experiments to an axisymmetric geometry over the past few years, for example, in the case of internal waves generated by plumes [20], or using an axisymmetric wave generator [21–23]. Some differences between the axisymmetric and the Cartesian case have been noted in the nonlinear dynamics, for example, regarding the generation of super-harmonics [24,25]. But the linear regime is similar in that the dispersion relation remains unchanged and naturally introduces a cutoff frequency for the waves, meaning that if their frequency is larger than the buoyancy frequency N, they are evanescent and cannot vertically propagate.

Transmission of internal waves across sharp and smooth interfaces between two layers of uniform N has been studied both in Cartesian [5,26] and axisymmetric [21] settings. Experimental measurements of velocity amplitudes have shown that, close to the transition region, the velocity is still nonzero although the wave frequency ω is above N. Propagating waves impinging on a weakly stratified layer of fluid sandwiched between two strongly stratified regions can get through this layer, in which they are evanescent, by a phenomenon known as tunneling [7,27].

In the present paper, building on a series of recent works on axisymmetric internal waves [8,21–23], we extend the previous study of Sutherland and Yewchuk [7] on Cartesian internal wave tunneling to the case of axisymmetric wave fields. We first investigate whether this change of geometry affects the tunneling phenomenon, and we then propose a quantitative investigation of the associated transmission coefficients. The theory of internal wave tunneling is developed in Sec. II with a simple three-layered model that allows for the computation of transmission coefficients and that can be further generalized. After describing the experimental and numerical methods in Sec. III, the theory is tested in Sec. IV with both qualitative and quantitative results. This section also puts the emphasis on the challenges set in accurately and reliably measuring internal wave amplitudes, especially in confined domains. We present a robust innovative method to reach this goal. Our conclusions and discussion are presented in Sec. V.

II. THEORY

A. Governing equations

Under the Boussinesq approximation, the linear internal wave equation in a nonrotating, inviscid density stratified fluid in an axisymmetric geometry is [21]

$$\frac{\partial^2}{\partial t^2}\left(\frac{\partial^2\psi}{\partial z^2}+\frac{\partial}{\partial r}\left(\frac{1}{r}\frac{\partial(r\psi)}{\partial r}\right)\right)=-N^2(z)\frac{\partial}{\partial r}\left(\frac{1}{r}\frac{\partial(r\psi)}{\partial r}\right), \tag{1}$$

where ψ is the stream function and $N(z)=(-g/\rho_0\mathrm{d}\bar{\rho}(z)/\mathrm{d}z)^{1/2}$ the buoyancy frequency, which is assumed to be a function of z only, with g the gravity constant, $\bar{\rho}$ the background density, and ρ_0 the reference density. The vertical and radial velocities, v_z and v_r, respectively, are given by spatial derivatives of the stream function ψ as follows:

$$v_z=\frac{1}{r}\frac{\partial(r\psi)}{\partial r}\quad\text{and}\quad v_r=-\frac{\partial\psi}{\partial z}. \tag{2}$$

Over parts of the stratification with constant buoyancy frequency N and considering a finite domain with a cylindrical boundary at a radius R, the analytical solution of Eq. (1) is a superposition of vertically propagating, radially standing, waves individually defined as

$$\psi(r,z,t)=\psi_0 J_1(lr)e^{i(mz-\omega t)}, \tag{3}$$

in which ψ_0 is a constant amplitude, l and m are the radial and vertical wave numbers, ω is the wave frequency, and J_1 is the first-order Bessel function of the first kind [22]. The radial wave number l is then imposed by boundary conditions at $r=R$ [22,23]. Inserted in the wave equation, this solution yields

$$m^2=l^2\left(\frac{N^2}{\omega^2}-1\right), \tag{4}$$

which implicitly defines the internal wave dispersion relation relating the frequency ω to the wave numbers l and m. This describes two kinds of waves: either $\omega<N$ and the waves are propagating (m real-values); or $\omega>N$ and the waves are evanescent (m is purely imaginary) in

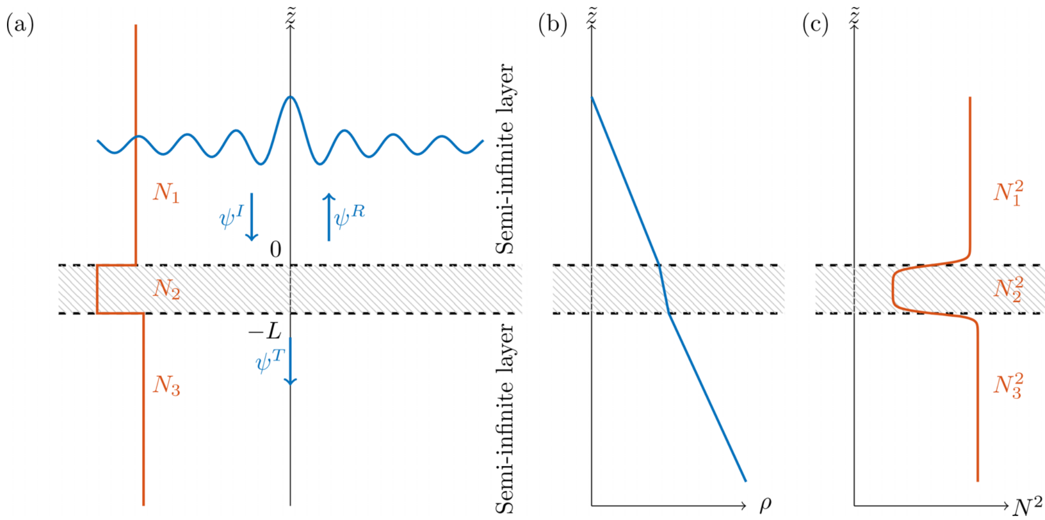

FIG. 1. Tunneling of a horizontal axisymmetric Bessel mode across a weakly stratified layer, represented by the hatched region between 0 and $-L$: (a) schematic of the phenomenon, where the blue pattern represents a Bessel-shaped wave field in the horizontal, with a free incident wave stream function ψ^I reaching the interface, leading to a reflected wave ψ^R and a transmitted wave ψ^T; (b) density profile of the stratification; (c) squared buoyancy frequency profile modeled using two hyperbolic tangents.

which case, according to Eq. (3), the wave amplitude decays exponentially in the vertical direction. The buoyancy frequency N therefore acts as a cutoff frequency.

B. Three-layered problem

We examine the transmission of a single axisymmetric wave [defined as in Eq. (3)] incident from above upon a three-layered piecewise-constant $N(z)$ profile given by

$$N(z) = \begin{cases} N_1 & \tilde{z} \geqslant 0 \\ N_2 & -L < \tilde{z} < 0 \\ N_3 & \tilde{z} \leqslant -L \end{cases}, \tag{5}$$

as depicted in Fig. 1. The vertical coordinate $\tilde{z}$ is defined such that the top interface is located at $\tilde{z} = 0$. We consider that the intermediate layer of buoyancy frequency N_2, for $\tilde{z} \in [-L; 0]$ (i.e., vertical extension $\Delta\tilde{z} = L$) is weakly stratified ($N_2 < N_1, N_3$). Henceforth, L refers to the thickness of this weakly stratified layer.

In a model case of sharp interfaces between the N_1, N_2, and N_3 regions, this equation can be solved independently in each layer and interrelated using interface conditions at $\tilde{z} = 0$ and $\tilde{z} = -L$ [7,21,28]. For $\tilde{z}$ in a given region of N_i, the stream function is $\psi_i = \hat{\psi}_i(\tilde{z}) J_1(lr) e^{-i\omega t}$ where $\hat{\psi}$ is the stream function amplitude. Considering downward propagating modes, the continuity of the pressure and vertical velocity fields implies that l and ω are conserved while transmission occurs across the sharp interfaces between the three regions [21].

Although each value of N_i is arbitrary, it is assumed in this study that the incident wave has a frequency smaller than N_1 and N_3, so that transmission is possible (i.e., the wave field is always propagating in the top and in the bottom layers, but not necessarily in between). The stream function amplitude in the top layer is a superposition of an incident and reflected wave: $\hat{\psi}_1 = A_I \exp(\imath m_1 \tilde{z}) + A_R \exp(-\imath m_1 \tilde{z})$, in which $m_1 = l(N_1^2/\omega^2 - 1)^{1/2}$. In the bottom layer, the stream function is composed of a downward propagating wave alone since this layer is assumed to have infinite depth: $\hat{\psi}_3 = A_T \exp(\imath m_3 \tilde{z})$, in which $m_3 = l(N_3^2/\omega^2 - 1)^{1/2}$. In the middle layer, two cases are considered:

(1) If $\omega < N_2$, the stream function amplitude is given by $\hat{\psi}_2 = B_1 \exp(\imath \gamma_+ \tilde{z}) + B_2 \exp(-\imath \gamma_+ \tilde{z})$, in which $\gamma_+ = l(N_2^2/\omega^2 - 1)^{1/2}$. Waves can propagate in this layer.

(2) If $\omega \geqslant N_2$, the stream function amplitude is given by the linear combination $\hat{\psi}_2 = B_1 \exp(\gamma_- \tilde{z}) + B_2 \exp(-\gamma_- \tilde{z})$, in which $\gamma_- = l(1 - N_2^2/\omega^2)^{1/2}$. Waves are evanescent in this layer, with exponentially varying amplitudes.

Continuity of the pressure and vertical velocity fields at the interfaces at $\tilde{z} = 0$ and $-L$ require continuity of the stream function amplitude and its derivative. This then gives four equations in the five unknown amplitudes A_I, A_R, A_T, B_1, and B_2. Applying the interface conditions thus gives the transmitted amplitude A_T in terms of the incident amplitude A_I. A fraction of the wave energy is reflected back into the upper domain (amplitude A_R) [21], depending on how much energy is transmitted through the layer.

C. Transmission coefficient

For both of the aforementioned cases, we now try to quantify how much of the wave field can be transmitted through the weakly stratified layer of buoyancy frequency N_2. As discussed in a previous study [21], it is possible to relate the transmitted, reflected, and incident wave fields using transmission and reflection coefficients. These coefficients are ratios that can be computed using different quantities, notably the vertical velocity, the radial velocity, or the energy of the wave field. The vertical and radial velocities are used here since they give complete access to the wave field while being the most practical to measure experimentally.

For the vertical velocity field v_z, the transmission coefficient T_{v_z} is given in terms of the ratio of $\partial_r \psi_T$ to $\partial_r \psi_I$, i.e., $T_{v_z} = (l_3/l_1)|A_T|/|A_I|$. The radial wave number is conserved across interfaces in such configurations, thus $l_1 = l_3$ and the transmission coefficient is directly given by the ratio of the stream function amplitudes A_T to A_I, explicitly $T_{v_z} = |A_T|/|A_I|$. We find the following coefficient:

$$T_{v_z} = \begin{cases} 2m_1\gamma_+\left[\left(m_1^2 - \gamma_+^2\right)\left(m_3^2 - \gamma_+^2\right)\sin^2(\gamma_+ L) \; + \; \gamma_+^2(m_1 + m_3)^2\right]^{-1/2}, & \text{if } \omega < N_2, \\ 2m_1\gamma_-\left[\left(m_1^2 + \gamma_-^2\right)\left(m_3^2 + \gamma_-^2\right)\sinh^2(\gamma_- L) \; + \; \gamma_-^2(m_1 + m_3)^2\right]^{-1/2}, & \text{if } \omega \geqslant N_2. \end{cases} \tag{6}$$

Interestingly, in the particular case $N_3 = N_1$, the square of T_{v_z} obtained here is analogous to the transmission coefficient for energy found by [7]. As for the radial velocity field v_r, which is computed using the negative z derivative of the stream function, the appropriate transmission coefficient is given by $T_{v_r} = (m_3/m_1)|A_T|/|A_I|$, or more explicitly, for $\omega < N_1$ and N_3,

$$T_{v_r} = \left(\frac{N_3^2/\omega^2 - 1}{N_1^2/\omega^2 - 1}\right)^{1/2} T_{v_z}. \tag{7}$$

In Eq. (6), the solution for $\omega < N_2$ corresponds to waves propagating in all layers, while the other expression for $\omega \geqslant N_2$ describes the tunneling case.

These transmission coefficients depend on various parameters that can be tuned in the experiments: the buoyancy frequencies N_1, N_2, and N_3, the forcing frequency ω, the radial wave number l, and the vertical extent of the evanescent region L. Taking N_3 to be approximately equal to N_1, these parameters collapse into three dimensionless variables ω/N_1, N_2/N_1, and $L \times l$. We can study their influence by plotting colormaps of the transmission coefficient, similarly to [7,21]. They are shown in Fig. 2 with T_{v_z} as a function of (a) ω/N_1 and N_1/N_2 at a given $L \times l = 0.76$, and (b) ω/N_1 and $L \times l$ at a given $N_2/N_1 = 0.45$. Both plots are produced using $N_3 = 1.1N_1$, as obtained experimentally in the next section. The choice of $L \times l = 0.76$ [in Fig. 2(a)] and of $N_2/N_1 = 0.45$ [in Fig. 2(b)] is also justified by the experimental conditions detailed below.

Three regions can be identified in the colormaps of Fig. 2, separated by a white dotted line and by a white dashed line. The leftmost part of the colormap corresponds to the resonant regime in which peaks of increased transmission amplitudes appear when ω/N comes closer to particular values, for

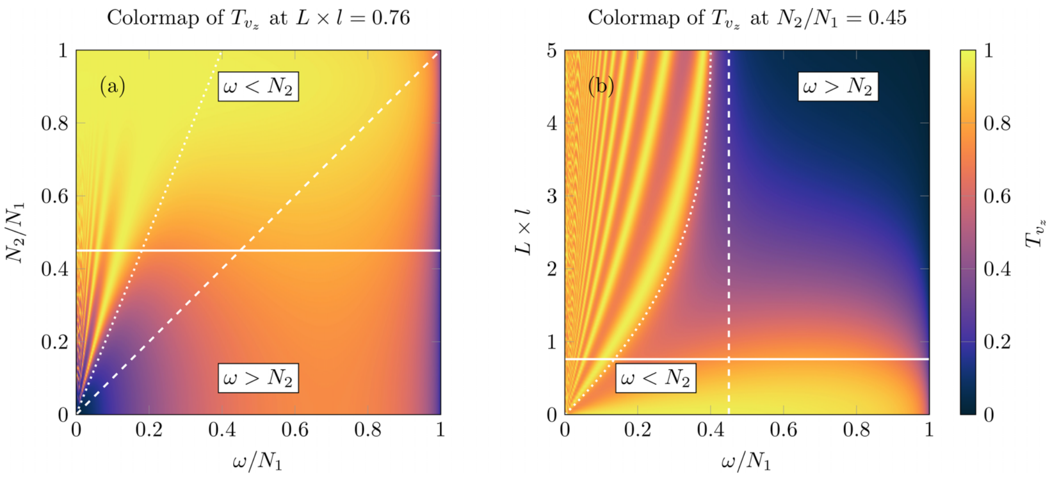

FIG. 2. Colormaps of the predicted transmission of vertical velocity T_{v_z} as: (a) a function of ω/N_1 and N_2/N_1 with $L \times l = 0.76$; and (b) of ω/N_1 and $L \times l$ with $N_2/N_1 = 0.45$. In both cases we set $N_3/N_1 = 1.1$. The white solid lines show the cuts at (a) $N_2/N_1 = 0.45$ and (b) $L \times l = 0.76$. The white dashed lines separate the evanescent ($\omega > N_2$) and the propagating ($\omega < N_2$) cases. The white dotted curves bounding the peaks to the leftmost part show the approximate limit between the resonant (with peaks in transmission) and the propagating cases.

example, when $\omega/N_1 \to 0.2$ for $L \times l = 0.76$ in Fig. 2(b). As evident in Fig. 2(a), these peaks are shifted to lower frequencies ω when the ratio N_2/N_1 or $L \times l$ decrease. This regime is characterized by resonances in the weakly stratified layer that form a cavity for the waves that behaves like a wave resonator [21,29], i.e., their successive reflections at the top and bottom interfaces lead to constructive or destructive interference in this layer. Since exact resonances (corresponding to the peaks in T_{v_z}) are obtained when the size of the layer (the cavity) is an integer multiple of the half-vertical wavelength [21,22], this regime exists only for vertical wavelengths smaller than $2L$. Considering $2L$ as the largest vertical wavelength allowed defines a lowest-order resonance relation that can be written either as

$$L \times l = \frac{4\pi}{\sqrt{\frac{N_2^2}{\omega^2} - 1}} \quad \text{at fixed } N_2/N_1 \text{ [in Fig. 2(a)]}, \tag{8}$$

or

$$\frac{N_2}{N_1} = \frac{\omega}{N_1}\sqrt{\left(\frac{4\pi}{L \times l}\right)^2 + 1} \quad \text{at fixed } L \times l \text{ [in Fig. 2(b)]}, \tag{9}$$

materialized in each panel of Fig. 2 by a white dotted curve. These equations were however obtained with a sharp interface model, which underestimates the size of the weakly stratified region compared to an effective size in the case of smooth interfaces. For this reason, this dotted curve represents a bounding limit of the actual resonance region.

The central region corresponds to the fully propagating regime: waves can propagate in all three layers, and no resonance effect is observed in the weakly stratified layer. The rightmost region, delimited by the white dashed line at $\omega/N_1 = N_2/N_1$, corresponds to the tunneling regime, in which waves cannot propagate in the weakly stratified layer. As can be seen in Fig. 2, increasing either the thickness of the weakly stratified layer L or the radial wave number l (i.e., $L \times l$) broadens the resonant region and reduces the propagating one. The frequency range corresponding to the tunneling regime ($\omega/N_1 \in [N_2/N_1; 1]$), remains unchanged since its definition only depends on the buoyancy frequencies.

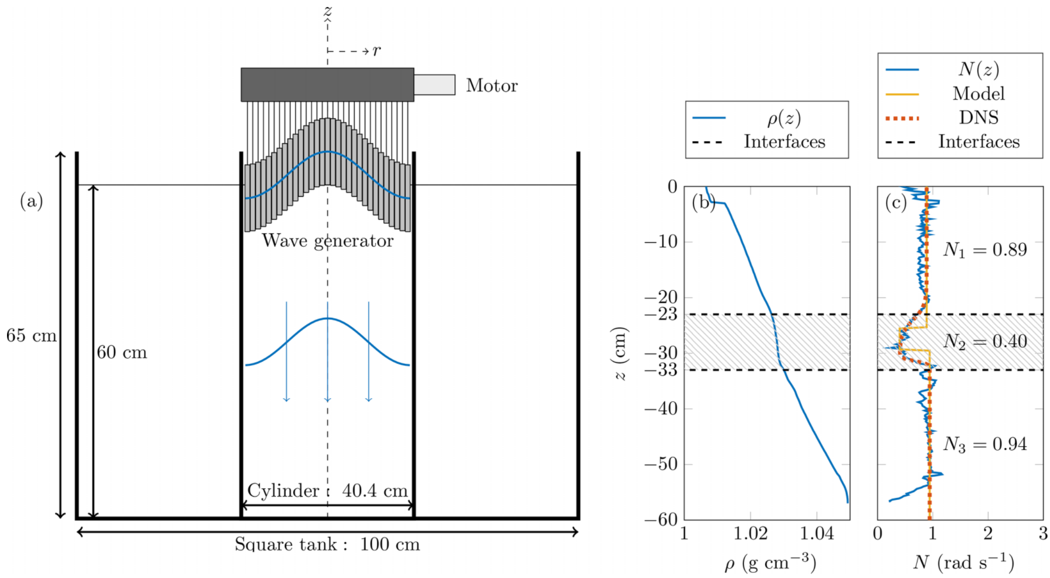

FIG. 3. (a) Schematic of the experimental apparatus in a vertical cross-section showing a cylindrical tank, inside a square tank, that confines the waves produced by the generator located at the surface, leading to a radial Bessel mode propagating downwards. The vertical dimension of the generator on this schematic is not to scale. (b) Density and (c) buoyancy frequency profiles from experiment 1 (solid blue line), piecewise-constant profile in the model (solid yellow line), and profile used in the simulations as given by Eq. (15) (dotted orange line). The hatched region between $z = -23$ cm and $z = -33$ cm corresponds to the weakly stratified layer identified from the density profile $\rho(z)$.

III. METHODS

A. Experimental apparatus

We conducted a set of experiments using the apparatus described in [21,22], adapted from the setup of Maurer *et al.* [23]. A general schematic of the experimental device is presented in Fig. 3. Throughout our study, we are using natural cylindrical (r, z) coordinates whose origin is taken at the water surface at the center of the tank. The z axis is thus redefined compared to $\tilde{z}$ used in the previous theoretical section.

The wave generator is made of 16, 12 mm thick, concentric PVC cylinders periodically oscillating, each of them being forced by two eccentric cams. The eccentricities can be configured to introduce a phase shift between the different cylinders, and the oscillating amplitude can be set for each individual cylinder. As a result, the vertical displacement of the n^{th} cylinder can be described by

$$a_n(t) = A_n \cos(\omega t + \alpha_n), \tag{10}$$

with A_n its vertical displacement amplitude, ω the forcing frequency, and α_n a phase shift. For a smooth motion of the PVC cylinders, a 1 mm gap is kept between each cylinder and the total radius of the wave generator is then $R = 201$ mm. The generator is mounted at the surface of the water to force downward propagating internal waves. The wave field is forced using a mode 1 profile in the horizontal direction, i.e., the radial wave number l satisfies $J_1(lR) = 0$, so that the radial velocity is zero at the imposed cylindrical boundary, with lR being equal to the first zero of the Bessel function J_1, $\xi_0 \simeq 3.83$. We thus use $l = \xi_0/R \simeq 19\,\mathrm{m}^{-1}$. The corresponding amplitudes of each cam are presented in Table I. This profile is efficient for generating axisymmetric Bessel-shaped wave fields [22].

TABLE I. Amplitudes of the different cams of the generator for a mode 1 radial profile. The first cam is located at $r = 0$.

Cams	1	2	3	4	5	6	7	8	9	10	11	12	13	14	15	16
Mode 1 amplitudes (mm)	2.5	2.4	2.3	2.1	1.9	1.6	1.3	0.9	0.6	0.2	−0.1	−0.3	−0.6	−0.8	−0.9	−1

Experiments were conducted in a cylindrical acrylic tank of the same inner diameter as the generator. This transparent cylindrical tank was set into a square acrylic tank to reduce distortions that would occur due to the curved interface created by the cylinder. Both tanks were filled with salt-stratified water with the same density profile. We adapted the double-bucket method [30,31] to fill the experimental tank with a layered stratification, using a stop-and-go method [21]. The density profile $\rho(z)$ was measured from the free surface to within a couple of centimeters of the bottom of the tank, using a calibrated PME conductivity and temperature probe mounted on a motorized vertical axis. The buoyancy frequency was estimated from the mean value of the $N(z)$ profile obtained from $\rho(z)$, smoothed over 2 cm. The wave generator was immersed at a depth of 2 cm into the stratification. The error on the buoyancy frequency was estimated using the standard deviation of this N profile, which was about 4% of the estimated N value (see [22] for more details).

As shown in Figs. 3(b) and 3(c), with the density and the buoyancy frequency profiles, respectively, we managed to create a nonlinear stratification that can be split into three regions, with $N_1 = 0.89 \pm 0.04\,\mathrm{rad\,s^{-1}}$ (top layer), $N_2 = 0.40 \pm 0.02\,\mathrm{rad\,s^{-1}}$ (intermediate, weakly stratified layer), and $N_3 = 0.94 \pm 0.04\,\mathrm{rad\,s^{-1}}$ (bottom layer) yielding $N_3/N_1 = 1.1$ and $N_2/N_1 = 0.45$ (as mentioned in the previous section). Given that N_1 and N_3 have similar values but with $N_1 < N_3$, we will then normalize all frequencies by N_1 which is the relevant parameter for waves propagating both in the top and bottom layers.

The density profile (similar to the one presented in Sutherland and Yewchuk [7]) shows a weakly stratified layer between $z = -23$ and -33 cm [hatched region in Figs. 3(b) and 3(c)] but, due to its smoothing, the buoyancy frequency profile rather suggests a thinner transition layer. In the theoretical model as well as in the design of the experiment, we consider infinitely sharp interfaces between the different layers but, experimentally, we can only obtain interfaces smoothed over 2 to 4 cm. We will thus retain a smaller characteristic thickness of $L = 4$ cm for the buoyancy frequency profile used in the model [yellow curve in Fig. 3(c)] and for plotting the theoretical curves. While discussing the experimental and numerical data, however, we should keep in mind that the weakly stratified layer is smoother and of a larger vertical extent. The relevant dimensionless quantity we will use is then $L \times l = 0.76$.

Because the tank is 60 cm tall, the vertical extent of each of the three layers of fluid is necessarily limited. The top and bottom layers in which a good visualization is required to measure the amplitudes should be significantly larger than the weakly stratified layer, partly in order to avoid disturbances introduced by the wave field reflected at the upper and lower boundaries of the domain. In the profile presented in Fig. 3, the weakly stratified layer extends over 7% to 17% of the available height ($L = 4$ cm and $L = 10$ cm, respectively). In this layer, the amplitude of the wave field decays if waves are evanescent ($\omega/N_1 > N_2/N_1 = 0.45$). The layer being relatively thin, we only expect a small decay of the velocity field amplitude when tunneling occurs. In fact, as shown in Fig. 2(b), increasing $L \times l$ (i.e., increasing the thickness of the weakly stratified layer at a fixed radial wave number l) would give a more significant decay and thus lower transmission coefficients. A useful consequence of this experimental limitation is the existence of a wide range of frequencies in the fully propagating case, nicely separating the resonant regime (with peaks in Fig. 2) from the tunneling one (obtained for ω such that $N_2 < \omega < N_1$). Since our interest lies in the tunneling regime and in its transition with the fully propagating one, we restrict our study to forcing $\omega/N_1 \in [0.2; 1]$.

Velocity fields were obtained via particle image velocimetry (PIV). A laser sheet was created by a laser beam (Ti:sapphire, 2 watts, wavelength 532 nm) going through a cylindrical lens. It could be oriented either horizontally (to measure the radial and orthoradial velocity) or vertically (to measure the vertical and the radial velocity). For the purpose of visualization, 10 µm diameter hollow glass spheres of volumetric mass 1.1 g cm^{-3} were added to the fluid while filling the tank. To obtain good-quality velocity fields near the bottom of the tank and while imaging in a horizontal plane, 10 µm silver-covered spheres of volumetric mass 1.4 g cm^{-3} were added when needed in some experiments. Images were recorded at 4 Hz and data processing of the PIV raw images was done using the CIVx algorithm [32]. Velocity fields were then filtered around the forcing frequency to improve the quality of the visualization. This processing was not applied while measuring amplitudes in order to prevent any loss of information.

B. Direct numerical simulations

A nonlinear model was used to simulate the transmission and reflection of axisymmetric waves from a localized region of relatively weak stratification. The code is adapted from that used by [33]. In particular, the axisymmetric Navier-Stokes equations in the Boussinesq approximation were numerically solved for the perturbation density, ρ, and the azimuthal component of vorticity, $\zeta = \partial_z v_r - \partial_r v_z$. The governing equations are

$$\frac{\partial \zeta}{\partial t} = -v_r r \frac{\partial}{\partial r}\left(\frac{\zeta}{r}\right) - v_z \frac{\partial \zeta}{\partial z} + \frac{g}{\rho_0}\frac{\partial \rho}{\partial r} + \nu \mathcal{D}_1 \zeta, \tag{11}$$

$$\frac{\partial \rho}{\partial t} = -v_r \frac{\partial \rho}{\partial r} - v_z \frac{\partial \rho}{\partial z} - v_z \frac{\partial \bar{\rho}}{\partial z} + \kappa \mathcal{D}_0 \rho, \tag{12}$$

in which v_r and v_z are the radial and vertical velocity, respectively, and g is gravity. The background and reference densities are denoted by $\bar{\rho}(z)$ and ρ_0. $\mathcal{F}_n$ are forcing operators, described below, and $\mathcal{D}_n$ is the Laplacian operator, given explicitly in axisymmetric cylindrical coordinates by

$$\mathcal{D}_n f = \frac{1}{r}\frac{\partial}{\partial r}\left(r \frac{\partial f}{\partial r}\right) - \frac{n^2 f}{r^2} + \frac{\partial^2 f}{\partial z^2}, \tag{13}$$

for $n = 0$ or 1, denoting the corresponding order of the Bessel function associated with the field, f. Here, we take $\nu = 0.01\,\mathrm{cm^2\,s^{-1}}$ and $\kappa = 0.0001\,\mathrm{cm^2\,s^{-1}}$. For reasons of numerical convergence, the diffusivity of density, κ, is chosen to be an order of magnitude larger than that of salt water. However, it is sufficiently small to ensure that diffusivity plays a negligible role in influencing the tunneling dynamics.

Given the vorticity at some time, the stream function ψ is found by inverting the vorticity equation

$$\mathcal{D}_1 \psi = -\zeta. \tag{14}$$

This was done by representing ψ and ζ as a discrete Fourier sine transform in the vertical and a discrete Bessel transform in the radial direction. The resulting algebraic equation was solved to find the transform coefficients for ψ, and these were then used to compute ψ in real space. The radial and vertical velocities, v_r and v_z, were then found using Eq. (2).

The governing equations are discretized and solved on a regular staggered grid with a second-order finite-difference scheme. The radial resolution and vertical resolution are both set to be $\simeq$0.2 cm. Free-slip, no-normal flow conditions are imposed at the top and bottom boundaries and at the outer radius. To transform and invert (14), the first 50 J_1 Bessel modes are used in the radial direction and a fast Fourier sine transform is used in the vertical. A fourth-order exponential wave number cutoff filter is used to suppress ringing in the transforms (see [33]). The prognostic equations are advanced in time using a leap-frog scheme in which time-splitting errors are minimized by performing an Euler backstep after 20 steps, with each step being 0.01 s. Simulations run with half the grid spacing and one quarter the time step confirmed that the dynamics were sufficiently well resolved.

At the start of a simulation, ζ and ρ are both set to zero everywhere, and the background stratification is prescribed through hyperbolic tangent functions, designed to approximate the stratification in the experiments. Explicitly,

$$N^2(z) = \frac{1}{2}\left(N_1^2 - N_2^2\right)\tanh\left(\frac{z - z_1}{\sigma_1}\right) + \frac{1}{2}\left(N_3^2 - N_2^2\right)\tanh\left(\frac{z - z_2}{\sigma_2}\right) + \frac{1}{2}\left(N_1^2 + N_1^2\right), \tag{15}$$

in which N_1 and N_3 are the buoyancy frequencies, respectively, above and below the region of reduced stratification, and N_2 captures the minimum buoyancy frequency ($N_2 < N_1, N_3$). The stratification is reduced for $z_2 \lesssim z \lesssim z_1 < 0$, with the transition from strong to weak stratification taking place over distances σ_1 (above) and σ_2 (below). Applying this modeling to experimental data, for the measured stratification shown in Fig. 3(c) (solid line), we set $N_1^2 = 0.79\,\mathrm{s}^{-2}$, ${N_3}^2 = 0.89\,\mathrm{s}^{-2}$, $N_2^2 = 0.16\,\mathrm{s}^{-2}$, $z_1 = -23.5\,\mathrm{cm}$, $z_2 = -31.5\,\mathrm{cm}$, $\sigma_1 = 2.5\,\mathrm{cm}$ and $\sigma_2 = 0.5\,\mathrm{cm}$ (dotted curve). Given N^2, the background density $\bar{\rho}$ is found by numerically integrating and setting the density to be ρ_0 at $z = 0$.

The effect of the forcing by the wave generator is established by prescribing the time change of ζ and ρ at $z = 0$. To ensure that the no-normal flow surface boundary condition prescribed at the top of the domain does not conflict with the imposed forcing, we extended the vertical size of the domain to $z = H$ and imposed the forcing at $z = 0$. If the vertical extent of the experiment spans $-H \leqslant z \leqslant 0$, the simulated domain thus has a vertical range $-H \leqslant z \leqslant H$. We then set $N(z) = N_1$ for $z \geqslant 0$, which allows waves to propagate upward while delaying reflections at the top and resonance effects in the upper layer beyond the total simulation time. At $z = 0$ and at each time t, the vertical displacement is taken to be $\xi = A_0 \sin(\omega t) J_0(lr)$, in which A_0 is the vertical displacement amplitude, ω is the forcing frequency and l is the radial wave number giving the mode's radial structure. From the polarization relations, the consequent time change of vorticity is prescribed by

$$\dot{\zeta}_f = -A_0 l N_1^2 \sin(\omega t) J_1(lr), \tag{16}$$

and the time change of the perturbation density is prescribed by

$$\dot{\rho}_f = A_0 \omega \left(\rho_0 N_1^2 / g\right) \cos(\omega t) J_0(lr). \tag{17}$$

Away from $z = 0$, the vorticity and perturbation density fields evolve in time according to (11) and (12), respectively. This leads to downward propagating waves below $z = 0$ and upward propagating waves above $z = 0$. During the simulation, the waves ultimately reflect from the top and bottom boundaries returning toward the source superimposed on the waves emanating from the source. The simulation is stopped before these reflected waves return to $z = 0$.

IV. RESULTS

In this section, we first present qualitative results providing evidence that axisymmetric internal waves can tunnel through the weakly stratified layer while conserving their modal shape; we then detail a method to accurately measure the amplitudes of the velocity fields associated to the waves and present quantitative measurements of the transmission coefficients for both the radial and vertical velocities, over a range of frequencies corresponding to both fully propagating and to tunneling waves.

A. Qualitative results: Wave fields

Figure 4 presents experimental velocity fields obtained via PIV. These show evidence of internal wave tunneling in the case of axisymmetric modes at sufficiently high frequencies. In the three cases, we see that the radial modal structure is established both in the top and bottom regions, indicating the presence of internal waves. The wave field at $\omega/N_1 = 0.34$ propagates through the three layers (frequency smaller than the buoyancy frequency of the weakly stratified region); those at

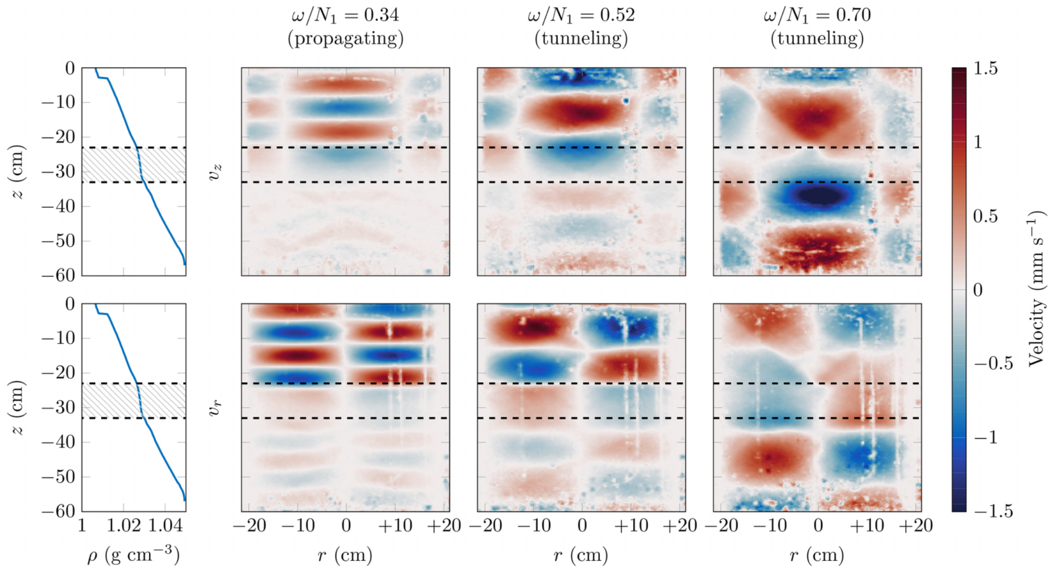

FIG. 4. Examples of experimental velocity fields for, from left to right: $\omega/N_1 = 0.34$, $\omega/N_1 = 0.52$, and $\omega/N_1 = 0.70$. The forcing amplitude is 2.5 mm at $r = 0$, yielding forcing vertical velocities of $0.76\,\mathrm{mm\,s^{-1}}$, $1.16\,\mathrm{mm\,s^{-1}}$, and $1.56\,\mathrm{mm\,s^{-1}}$, respectively. The first row is the vertical velocity and the second row is the radial velocity, from PIV fields filtered at the forcing frequency. Fields are taken 120 s after the generator has been started, when the wave field is fully established. The leftmost plots show the stratification (density profile, in solid blue) and the intermediate layer (hatched region) for reference; we have $N_2/N_1 = 0.45$.

$\omega/N_1 = 0.52$ and $\omega/N_1 = 0.70$ are tunneling through (frequency larger than the buoyancy frequency of the weakly stratified region, $N_2/N_1 = 0.45$). The velocity amplitudes are higher in the top region, partly because of the successive reflections.

As predicted by the theory, we see that, qualitatively, the radial modal structure is preserved in each layer but the amplitudes have decreased in the bottom layer due to the partial transmission across the weakly stratified region. Figure 5 presents horizontal profiles of the vertical and radial velocity fields above and below this layer, in the experiment at $\omega/N_1 = 0.70$, corresponding to the rightmost column of Fig. 4. On the profiles, taken at $z \simeq -10$ cm and at $z \simeq -40$ cm for the above and below cuts, are superimposed the fits from the expected Bessel functions, respectively, $J_0(lr)$ for the vertical velocity and $J_1(lr)$ for the radial velocity, with $l = 19\,\mathrm{m}^{-1}$ as set by the generator. Qualitatively, the fits agree well with the experimental profiles in both the top and bottom layers, confirming that the modal structure is well preserved while tunneling occurs. Some discrepancies can be noted, but are mostly due to reflections on the walls of the tank (e.g., for the peaks at 10 cm in the radial velocity profiles (c) and (d), also clearly visible in Fig. 4).

Similar qualitative results are obtained in the numerical simulations. Figure 6 shows snapshots of the velocity fields obtained in the DNS for $\omega/N_1 = 0.34$, $\omega/N_1 = 0.52$, and $\omega/N_1 = 0.70$. Once again, these snapshots show the existence of a velocity field both in the upper and in the lower layers, while showing the influence of the intermediate weakly stratified layer. This layer can be seen, in particular, in the radial velocity field at $\omega/N_1 = 0.34$ in which we note a velocity almost equal to zero around 30 cm deep. The snapshots at $\omega/N_1 = 0.52$, and $\omega/N_1 = 0.70$ indicate that waves are indeed tunneling through the weakly stratified layer, in agreement with the experimental data shown in Fig. 4. The qualitative comparison between Figs. 5 and 6 is, however, limited by a key difference in the setup: at the top boundary ($z = 0$), the wave field is reflected back in the experiment, yielding higher velocity amplitudes, whereas waves are damped in the upper part of the domain ($z > 0$) in the simulations, to avoid these reflections. This effect is enhanced for small values of ω/N_1 since the lower group velocity delays the tunneling effect.

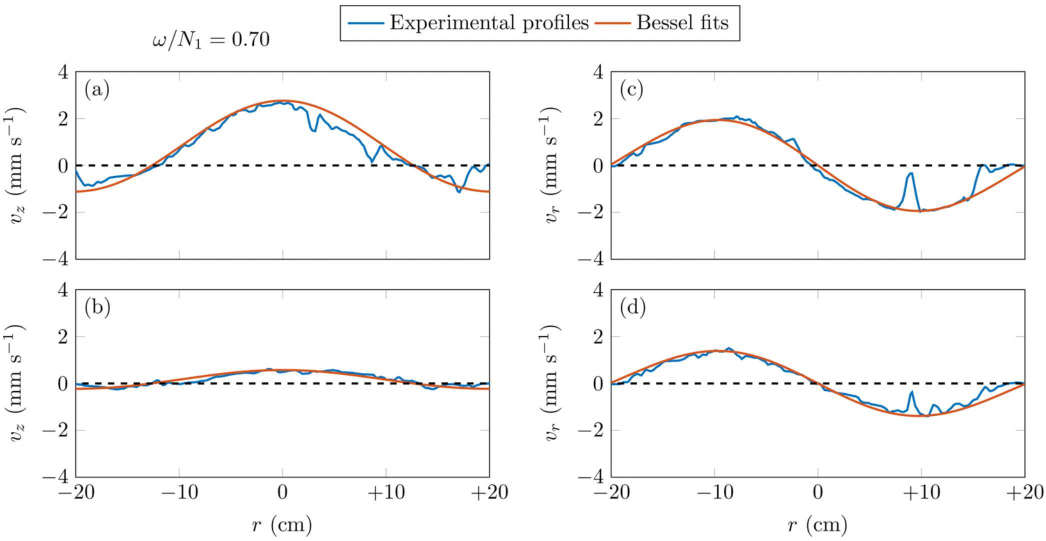

FIG. 5. Experimental profiles and fits by Bessel functions for $\omega/N_1 = 0.70$, with: (a) vertical velocity in the top layer, at $z \simeq -10$ cm; (b) vertical velocity in the bottom layer, at $z \simeq -40$ cm; (c) radial velocity in the top layer, at $z \simeq -10$ cm; (d) radial velocity in the bottom layer, at $z \simeq -40$ cm. Profiles are taken 70 s after the generator was started, before reflections fully established the cavity-modal structure.

B. Quantitative results: Amplitude measurements

To investigate in more detail the effect of the low buoyancy frequency region on the amplitude of the waves and to validate our transmission model, we run a set of experiments for forcings from

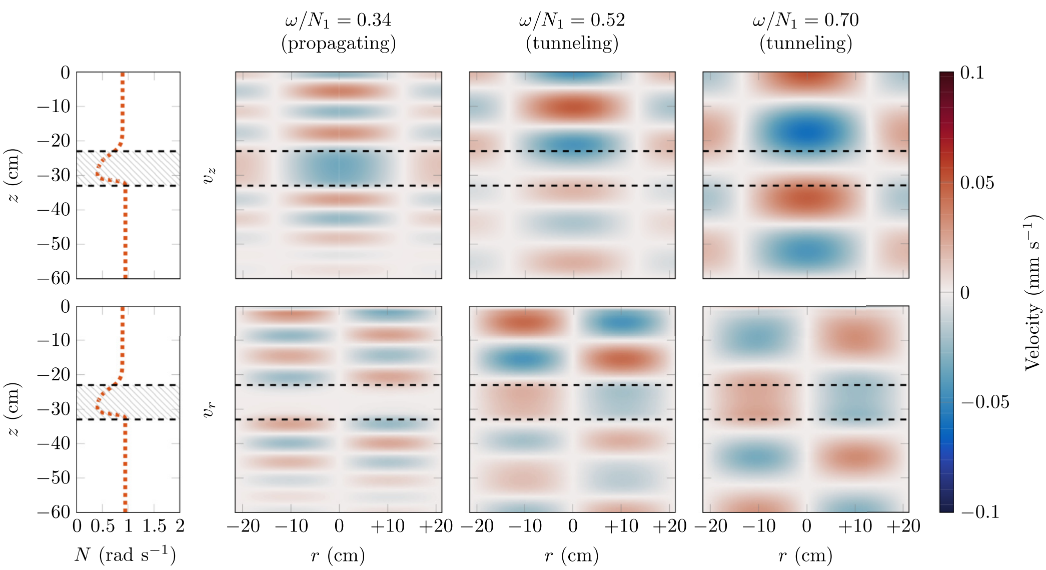

FIG. 6. Examples of numerical velocity fields for, from left to right: $\omega/N_1 = 0.34$, $\omega/N_1 = 0.52$, and $\omega/N_1 = 0.70$. The first row is the vertical velocity and the second row is the radial velocity. Fields are taken at $t_f = 120$ s after the generator has been started, when the wave field is fully established. The leftmost plots show the stratification (buoyancy profile, in dotted orange) and the intermediate layer (hatched region) for reference.

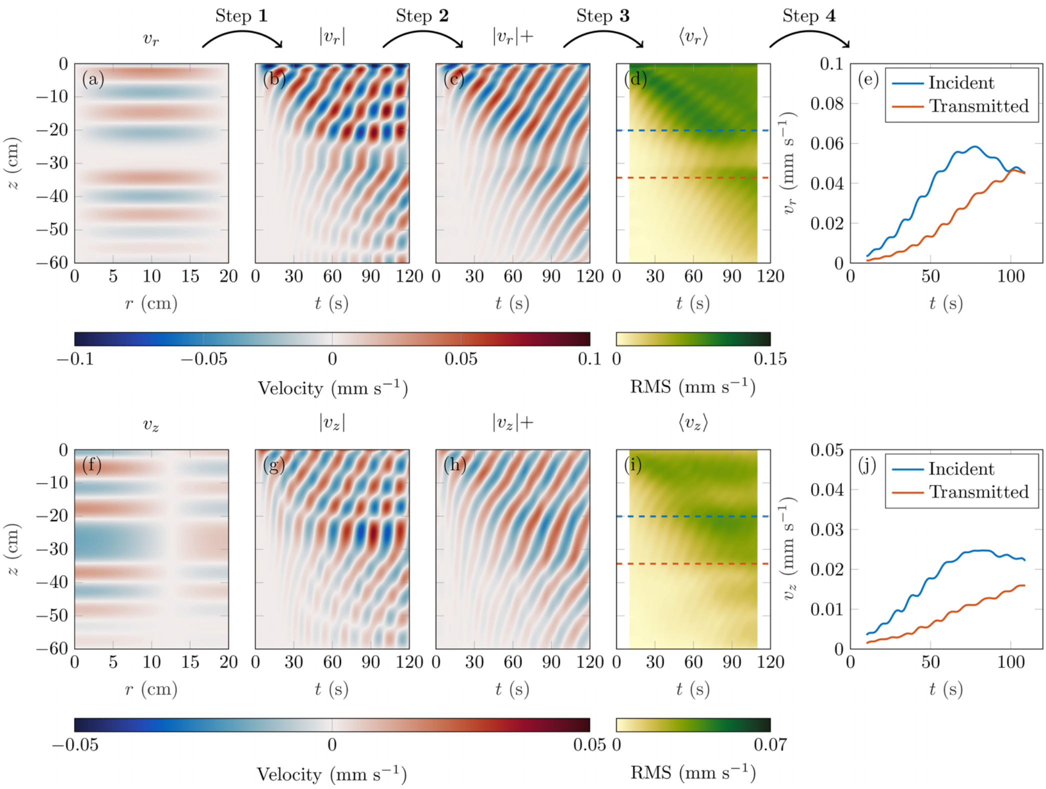

FIG. 7. Results from a numerical simulation for $\omega/N_1 = 0.34$, with the top row showing values for the radial velocity v_r and the bottom row showing values for the vertical velocity v_z. Steps 1 to 4 are explicited in the text. From left to right: (a) and (f) are snapshots of the radial and vertical velocity fields; (b) and (g) are space-time plots of the amplitude of the velocities; (c) and (h) are the corresponding Hilbert-transform-filtered time series showing only downward propagating waves; plots (d) and (i) show the time series constructed from the root-mean-square of the Hilbert-transformed time series shown in (c) and (h), respectively; and the graphs in (e) and (j) correspond to the values of the amplitudes from (d) and (i) computed for incident (blue) and transmitted (orange) waves at the levels indicated by the correspondingly colored horizontal dashed lines.

$\omega/N_1 = 0.18$ to $\omega/N_1 = 0.86$, which includes both frequencies for waves propagating in the entire stratification (i.e., smaller than $N_2/N_1 = 0.45$) and for waves evanescent in the weakly stratified layer (i.e., larger than N_2/N_1). According to the results of Fig. 4, waves are detected in the bottom region for all tested frequencies, both in the propagating and in the evanescent regimes. Our goal now is to estimate the transmission coefficients for v_z and v_r and compare them to the theoretical prediction of Eq. (6).

We developed an innovative technique to reliably perform amplitude measurements. We first tested this method with our DNS before applying it to our experimental data set. The principle of the whole process is detailed in Fig. 7 for the simulation at $\omega/N_1 = 0.34$, in which the different steps 1 to 4 are the following:

(1) We start by converting the series of snapshots of the vertical and radial velocity fields into a time series of the velocity field amplitudes. This is done by using the values of v_z and v_r at the expected maxima of the Bessel profiles giving the theoretical shape of the modal wave field, as shown in Fig. 5 (explicitly, at $r = 0$ cm for v_z ($J_0(lr)$) and at $r = 12.7$ cm for v_r ($J_1(lr)$)). Snapshots of v_z and v_r at $t = 120$ s are reproduced in panels 7(a) and 7(f), respectively. We only show the domain $0 \leqslant r \leqslant 20$ cm (half cylinder) for $-60 \leqslant z \leqslant 0$ cm (full vertical size of the domain), as the

other part for negative r can be obtained by symmetry. The space-time diagrams of the magnitudes of the velocities are shown in panels 7(b) and 7(g).

(2) These diagrams are then Hilbert transformed [34] to separate the downward propagating waves from the upward propagating ones. We retain the time series corresponding to downward propagating waves (with positive vertical wave number), which are shown in panels 7(c) and 7(h).

(3) From the Hilbert-transformed time series of downward propagating waves, a root-mean-square running average is computed over a time window T of duration equal to one period of the waves ($T = 2\pi/\omega$). The result is then multiplied by $\sqrt{2}$ so that values represent the half peak-to-peak amplitude of the fields as they depend on time and vertical location. The output, computed from panels 7(c) and 7(h), is shown in panels 7(d) and 7(i).

(4) By extracting horizontal slices through these images 7(d) and 7(i) just above and just below the weakly stratified region (as indicated by the dashed lines), we thus estimate the amplitude of the incident and transmitted waves as they vary in time. The temporal evolution of these amplitudes is shown in panels 7(e) and 7(j). The transmission coefficient is thus computed as the ratio of the maximum (in time) of the transmitted wave amplitude to the maximum of the incident wave amplitude for both the radial and vertical velocity fields, taken before a given time t_f. Computed using the group velocity in the top layer, this returning time is an estimate of the time after which waves have been reflected at the bottom and at the top of the tank. Such reflections introduce additional components in the raw velocity fields that cannot be straightforwardly isolated and that therefore disturb the measurement process.

The same processing is applied to the experimental data set. In Fig. 8, we present an example with the same frequency $\omega/N_1 = 0.34$ (which is more explicit than at higher frequencies), showing steps 1 to 4 from the raw velocity fields to the incident and transmitted wave amplitudes. Note that we see, in the second half of the experiment in panels 8(c) and 8(h), the appearance of nonlinear effects. To better estimate the velocity amplitudes, we use 10 consecutive horizontal cuts around the upper boundary of the weakly stratified layer, and 10 consecutive horizontal cuts around its lower boundary (i.e., cuts over about 2 cm above and below), giving $10 \times 10 = 100$ different combinations of cuts and as many transmission coefficients over which we take the mean value and the standard deviation. The final estimate thus becomes independent of the precise location and provides a confidence interval.

Measurements of the transmission coefficient are presented in Fig. 9 for both the vertical and radial velocities, T_{v_z} and T_{v_r}, with blue and orange circles, respectively. For each frequency, the value displayed is the mean over the 100 transmission coefficients computed, and the error bar is the standard deviation. Numerical data are superimposed for comparison (diamond symbols). The solid lines show the theoretical curves, obtained thanks to Eq. (6). The theoretical curve for the transmission coefficient of the vertical velocity, T_{v_z} (in blue), corresponds to the cuts indicated by dashed lines in the colormaps of Figs. 2(a) and 2(b). The parameters for the theoretical curves have been set to $N_1 = 0.89\,\mathrm{rad\,s^{-1}}$, $N_2 = 0.40\,\mathrm{rad\,s^{-1}}$, and $N_3 = 0.94\,\mathrm{rad\,s^{-1}}$ and $L = 4\,\mathrm{cm}$, in agreement with the stratification presented in Fig. 3. A vertical dotted line indicates the separation between the resonant and the fully propagating regimes; a vertical dashed line shows the cutoff frequency $N_2/N_1 = 0.45$ that separates the fully propagating from the tunneling regimes (as in Fig. 2). We note an excellent agreement between the numerical and experimental measurements. The same trend is observed for both radial and vertical velocity transmission, with a slightly larger transmission coefficient in the case of the horizontal radial velocity. Interestingly, our measurements confirm that there is a smooth transition between the fully propagating and tunneling cases around N_2/N_1.

V. CONCLUSIONS AND DISCUSSION

In this study, we have presented both experimental and numerical evidence of a tunneling effect for internal wave modes in axisymmetric geometry. This work notably extends the findings on Cartesian internal wave tunneling [7], in which 2D plane waves were considered, by focusing on three-dimensional, axisymmetric modes. This work is also complementary to the surveys on

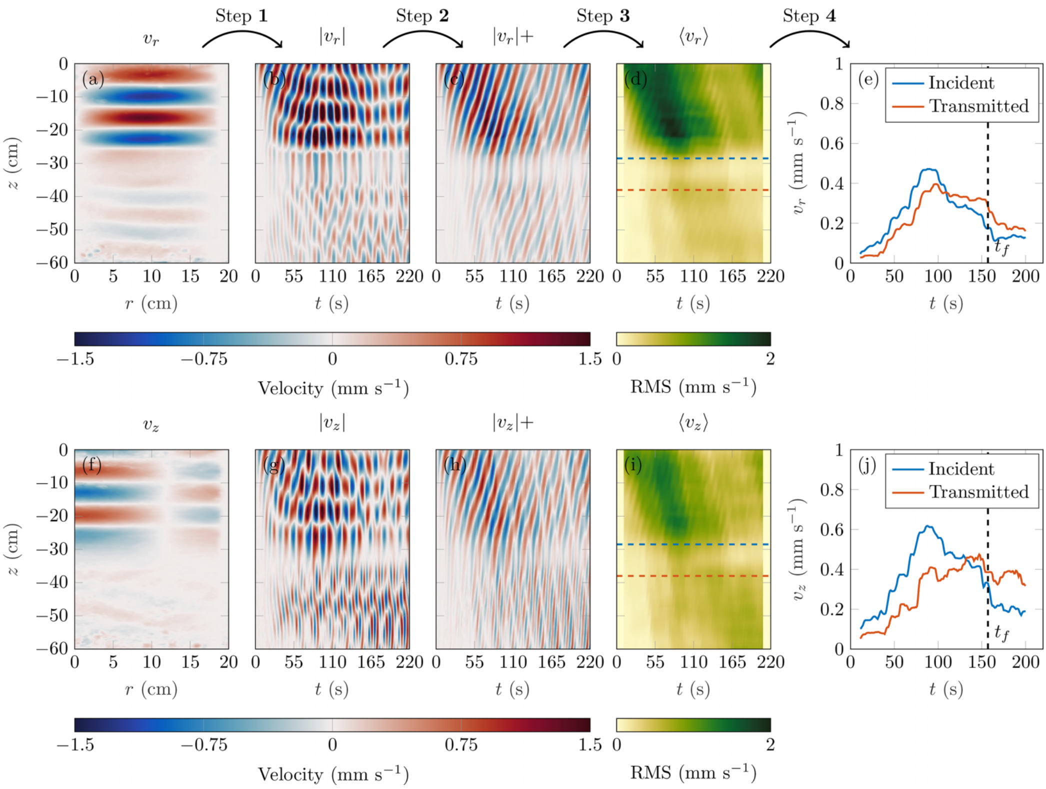

FIG. 8. Results from the processing of an experiment run at $\omega/N_1 = 0.34$, with the top row showing values for the radial velocity and the bottom row showing values for the vertical velocity. Panels (a) through (j) correspond to the steps 1 through 4 aforementioned and previously described in the caption of Fig. 7. In (e) and (j), the returning final time t_f is indicated by a vertical dashed line.

the transmission of axisymmetric internal wave modes across buoyancy interfaces (e.g., [21]), showing that such waves are indeed capable of tunneling through weakly stratified layers (or even homogeneous layers), similarly to plane waves. As such, it contributes to broadening our understanding of the complexity of highly stratified oceans, such as the Arctic, and of the possible impacts of energy transfers on their (re)stratification. Here, we first derived a simple model of transmission across a three-layered stratification in the case of a low buoyancy frequency intermediate layer and provided numerical and experimental measurements of internal wave amplitudes in such framework. Qualitatively, we have shown that downward propagating axisymmetric internal waves can tunnel through a weakly stratified layer while conserving their radial modal structure. This behavior is similar to the observed tunneling effect in Cartesian geometry, meaning that the change of geometry and energy distribution does not impact the linear dynamics of the waves. Quantitatively, we have found that these measurements of the transmission coefficients in vertical and radial velocity agree well with the theoretical prediction. Notably, our detailed measurements show that there exists a smooth transition between the fully propagating and the tunneling situations in terms of transmission coefficients. This suggests that internal waves are ultimately weakly affected by the presence of variations of relatively short vertical extension in the stratification.

Validating the theoretical model requires accurate measurements of the wave amplitudes both above and below the transition layer, in order to compute the transmission coefficients in velocity by taking the ratio of amplitudes. These measurements are usually challenging to obtain in internal

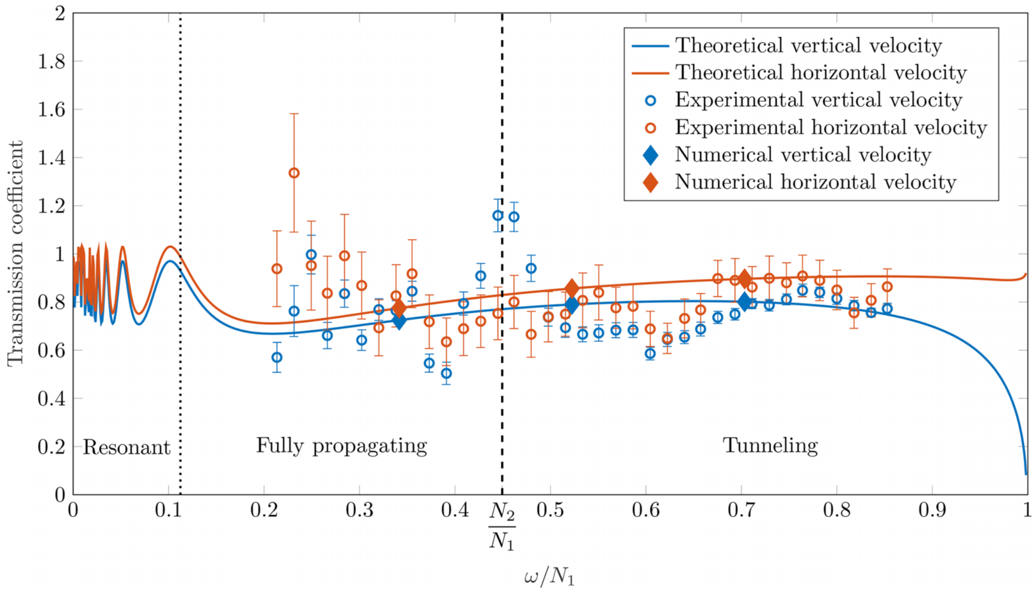

FIG. 9. Predicted transmission of vertical (solid blue) and horizontal (solid orange) velocities, compared to measurements of the transmitted vertical (blue circles) and horizontal (orange circles) velocities from experiment 1. Numerical data obtained with the same stratification are also indicated (diamond symbols). The theoretical curves correspond to the cuts indicated by the solid white lines in the colormaps of Figs. 2(a) and 2(b) and are computed for an intermediate layer of thickness $L = 4\,\mathrm{cm}$.

wave studies and even more in the present context due to the highly confined geometry and the short time window available. We thus developed and tested a technique based on nonlocal measurements, Hilbert filtering, and root mean square averaging. This innovative method proved to be very robust and allowed us to extract transmission coefficients from both the numerical and the experimental datasets, with very similar results, and therefore constitutes an interesting tool for future studies on internal waves.

Further work can be undertaken to complement this study. Direct numerical simulations such as those presented in Fig. 4 can be used to provide additional measurements of the transmission coefficients at various frequencies, using the same method, to check the relevance of the model. Possible resonant interference in the weakly stratified layer could be studied to determine whether they contribute significantly to the transmission coefficient (as was the case for a buoyancy frequency interface, see [21]). The transition between the intervals $\omega < N_2 < N_1$ and $N_2 < \omega < N_1$ could also be explored in more detail in the case of a finite top region, with a theory involving doubly confined layers and constructive-destructive interference behaviors in the top two layers of the stratification.

ACKNOWLEDGMENTS

This work has been partially supported by ANR Grant No. ANR-17-CE30-0003 (DisET) and by ONR Physical Oceanography Grant No. N000141612450. Data processing has been done thanks to the PSMN at the ENS de Lyon.

[1] B. Gayen and S. Sarkar, PSI to turbulence during internal wave beam refraction through the upper ocean pycnocline, Geophys. Res. Lett. **41**, 8953 (2014).
[2] S. J. Ghaemsaidi, S. Joubaud, T. Dauxois, P. Odier, and T. Peacock, Nonlinear internal wave penetration via parametric subharmonic instability, Phys. Fluids **28**, 011703 (2016).
[3] M. S. Paoletti and H. L. Swinney, Propagating and evanescent internal waves in a deep ocean model, J. Fluid Mech. **706**, 571 (2012).
[4] D. Varma, C. Pacary, T. Dauxois, and S. Joubaud, Experimental study of superharmonic internal wave resonant triads in finite-depth non-uniform stratifications, Phys. Rev. Fluids **9**, 094806 (2024).
[5] S. J. Ghaemsaidi, H. V. Dosser, L. Rainville, and T. Peacock, The impact of multiple layering on internal wave transmission, J. Fluid Mech. **789**, 617 (2016).
[6] B. R. Sutherland, Excitation of superharmonics by internal modes in non-uniformly stratified fluid, J. Fluid Mech. **793**, 335 (2016).
[7] B. R. Sutherland and K. Yewchuck, Internal wave tunnelling, J. Fluid Mech. **511**, 125 (2004).
[8] S. Boury, R. Supekar, E. C. Fine, R. Musgrave, J. B. Mickett, G. Voet, P. Odier, T. Peacock, J. A. Mackinnon, and M. Alford, Observations of double diffusive staircase edges in the Arctic Ocean, J. Geophys. Res.: Oceans **127**, e2022JC018906 (2022).
[9] O. M. Johannessen and O. S. Lee, Thermohaline staircase structure in the Tyrrhenian sen, Deep-Sea Res. **21**, 629 (1974).
[10] R. Molcard and A. J. Williams, Deep-stepped structure in the Tyrrhenian sea, Mémoires de la Société Royale des Sciences de Liège **6**, 191 (1975).
[11] R. B. Lambert, Jr. and W. Sturges, A thermohaline staircase and vertical mixing in the thermocline, Deep Sea Res. **24**, 211 (1977).
[12] P. A. Mazeika, Subsurface mixed layers in the northwest tropical Atlantic, J. Phys. Oceanogr. **4**, 446 (1974).
[13] R. W. Schmitt, H. Perkins, J. D. Boyd, and M. C. Stalcup, C-SALT: An investigation of the thermohaline staircase in the western tropical north Atlantic, Deep Sea Res. Part A **34**, 1655 (1987).
[14] L. Rainville and P. Winsor, Mixing across the Arctic Ocean: Microstructure observations during the Beringia 2005 expedition, Geophys. Res. Lett. **35**, 2008GL033532 (2008).
[15] M.-L. Timmermans, S. Cole, and J. Toole, Horizontal density structure and restratification of the Arctic Ocean surface layer, J. Phys. Oceanogr. **42**, 659 (2012).
[16] M.-L. Timmermans, J. Toole, R. Krishfield, and P. Winsor, Ice-tethered profiler observations of the double-diffusive staircase in the Canada basin thermocline, J. Geophys. Res. **113**, 2008JC004829 (2008).
[17] R. A. Woodgate, K. Aagaard, J. H. Swift, W. M. Jr. Smethie, and K. K. Falkner, Atlantic water circulation over the Mendeleev Ridge and Chukchi Borderland from thermohaline intrusions and water mass properties, J. Geophys. Res. **112**, C02005 (2007).
[18] L. Rainville, C. M. Lee, and R. A. Woodgate, Impact of wind-driven mixing in the Arctic Ocean, Oceanography **24**, 136 (2011).
[19] L. Rainville and R. A. Woodgate, Observations of internal wave generation in the seasonally ice-free Arctic, Geophys. Res. Lett. **36**, 2009GL041291 (2009).
[20] J. K. Ansong and B. R. Sutherland, Internal gravity waves generated by convective plumes, J. Fluid Mech. **648**, 405 (2010).
[21] S. Boury, P. Odier, and T. Peacock, Axisymmetric internal wave transmission and resonance in non-linear stratifications, J. Fluid Mech. **886**, A8 (2020).
[22] S. Boury, T. Peacock, and P. Odier, Excitation and resonant enhancement of axisymmetric internal wave modes, Phys. Rev. Fluids **4**, 034802 (2019).
[23] P. Maurer, S. J. Ghaemsaidi, S. Joubaud, T. Peacock, and P. Odier, An axisymmetric inertia-gravity wave generator, Exp. Fluids **58**, 143 (2017).
[24] L. E. Baker and B. R. Sutherland, The evolution of superharmonics excited by internal tides in non-uniform stratification, J. Fluid Mech. **891**, R1 (2020).
[25] S. Boury, T. Peacock, and P. Odier, Experimental generation of axisymmetric internal wave super-harmonics, Phys. Rev. Fluids **6**, 064801 (2021).

[26] R. Supekar and T. Peacock, Interference and transmission of spatiotemporally locally forced internal waves in non-uniform stratifications, J. Fluid Mech. **866**, 350 (2019).

[27] G. L. Brown and B. R. Sutherland, Internal wave tunnelling through non-uniformly stratified shear flow, Atmos. Oceans **45**, 47 (2007).

[28] P. G. Drazin and W. H. Reid, *Hydrodynamic Stability* (Cambridge University Press, Cambridge, 1981).

[29] M. Mathur and T. Peacock, Internal wave interferometry, Phys. Rev. Lett. **104**, 118501 (2010).

[30] J. M. H. Fortuin, Theory and application of two supplementary methods of constructing density gradient columns, J. Polym. Sci. **44**, 505 (1960).

[31] G. Oster and M. Yamamoto, Density gradient techniques, Chem. Rev. **63**, 257 (1963).

[32] A. Fincham and G. Delerce, Advanced optimization of correlation imaging velocimetry algorithms, Exp. Fluids **29**, S013 (2000).

[33] G. Voelker, P. G. Myers, M. Walter, and B. R. Sutherland, Generation of oceanic internal gravity waves by a cyclonic surface stress disturbance, Dyn. Atmos. Ocean. **86**, 116 (2019).

[34] M. Mercier, N. Garnier, and T. Dauxois, Reflection and diffraction of internal waves analyzed with the hilbert transform, Phys. Fluids **20**, 086601 (2008).